Exp.-Nr. **A2**
Eingang:
an PAC:

Mainz Microtron MAMI

A2 Collaboration at MAMI
Spokespersons: P. Pedroni, A. Thomas

Proposal for an Experiment

"Neutron Polarizabilities"

Spokespersons for the Experiment :

P.P. Martel (Institut für Kernphysik, Mainz, Germany
and Mount Allison University, Sackville, NB, Canada)
D. Hornidge (Mount Allison University, Sackville, NB, Canada)
E. Downie (George Washington University, Washington, DC, USA)

Abstract of Physics :

The polarizabilities of the proton have been studied extensively in the A2 Collaboration at MAMI, resulting in both a large improvement to the extraction of the scalar polarizabilities from a single experiment, as well as the first experimental extraction of the individual spin polarizabilities. To now study the neutron polarizabilities, we are proposing to measure the unpolarized differential cross section of Compton scattering off of both deuterium and helium, providing a significant improvement to the currently published data. An extraction using a Chiral Effective Field Theory calculation will push the errors of the neutron scalar polarizabilities closer to those of the proton, and pave the way for studying the neutron spin polarizabilities in the future.

Abstract of Equipment :

The experiment will be performed at the tagged photon facility of MAMI using the Crystal Ball and TAPS calorimeters together with the particle identification detector (PID) and multi-wire proportional chambers (MWPCs) for charged particle detection.

MAMI Specifications :

beam energy	883 MeV
beam polarization	unpolarized

Photon Beam Specifications :

tagged energy range	40 – 820 MeV
photon beam polarization	linearly polarized (145 MeV coherent edge)

Equipment Specifications :

detectors	Crystal Ball/TAPS, PID, MWPCs
targets	liquid deuterium and liquid helium

Beam Time Request :

set-up/test with beam	20 hours
data taking	980 hours

List of participating authors:

- **Institut für Physik, University of Basel, Switzerland**
  D. Ghosal, N. Jermann, A. Kaeser, B. Krusche, C. Meier
- **Institut für Experimentalphysik, University of Bochum, Germany**
  G. Reicherz
- **Helmholtz–Institut für Strahlen- und Kernphysik, University of Bonn, Germany**
  F. Afzal, R. Beck, A. Thiel, Y. Wunderlich
- **JINR, Dubna, Russia**
  N.S. Borisov, I. Gorodnov, A. Lazarev, A. Neganov, Yu.A. Usov
- **SUPA School of Physics and Astronomy, University of Glasgow, UK**
  J.R.M. Annand, S.Gardner, K. Livingston, I.J.D. MacGregor
- **Racah Institute of Physics, Hebrew University of Jerusalem, Israel**
  G. Ron
- **Kent State University, Kent, USA**
  D.M. Manley
- **Institut für Kernphysik, University of Mainz, Germany**
  P. Achenbach, M. Biroth, F. Cividini, A. Denig, P. Drexler, M.I. Ferretti-Bondy, W. Gradl, L. Heijkenskjöld, V.L. Kashevarov, P.P. Martel, E. Mornacchi, M. Ostrick, V. Sokhoyan, C. Sfienti, M. Thiel, A. Thomas, S. Wagner, J. Wettig
- **University of Massachusetts, Amherst, USA**
  R. Miskimen
- **Institute for Nuclear Research, Moscow, Russia**
  G. Gurevic
- **INFN Sezione di Pavia, Pavia, Italy**
  A. Braghieri, S. Costanza, P. Pedroni
- **Department of Physics, University of Regina, Canada**
  G.M. Huber
- **Mount Allison University, Sackville, Canada**
  D. Hornidge
- **George Washington University, Washington, USA**
  W.J. Briscoe, E.J. Downie, I.I. Strakovsky
- **Department of Physics, University of York, UK**
  M. Bashkanov, D.P. Watts, D. Werthmüller
- **Rudjer Boskovic Institute, Zagreb, Croatia**
  M. Korolija

1 Introduction

If a particle without internal structure is subjected to an electric or magnetic field, the response would only depend upon the particle's mass m, electric charge e, and anomalous magnetic moment κ, as given in the following two effective Hamiltonians

$$H_{\text{eff}}^{(0)} = \frac{\vec{\pi}^2}{2m} + e\phi \qquad H_{\text{eff}}^{(1)} = -\frac{e(1+\kappa)}{2m}\,\vec{\sigma}\cdot\vec{H} - \frac{e(1+2\kappa)}{8m^2}\,\vec{\sigma}\cdot\left[\vec{E}\times\vec{\pi} - \vec{\pi}\times\vec{E}\right], \quad (1)$$

where $\vec{\pi} = \vec{p} - e\vec{A}$. For a nucleon, which has an internal structure, additional terms called polarizabilities describe the internal response to these fields. At second order in this expansion,

$$H_{\text{eff}}^{(2)} = -4\pi\left[\frac{1}{2}\alpha_{E1}\vec{E}^2 + \frac{1}{2}\beta_{M1}\vec{H}^2\right], \quad (2)$$

the scalar polarizabilities α_{E1} and β_{M1} essentially describe how the nucleon stretches and aligns in an electric and magnetic field, respectively. At higher energies, additional terms play a role, including the next order terms called the spin, or vector, polarizabilities.

Since a photon is simply an electromagnetic wave, these polarizabilities can be experimentally accessed with nuclear Compton scattering. Different combinations of photon and target polarizations give rise to different observables which can, especially in the case of the spin polarizabilities, access terms with varying sensitivities.

1.1 Proton Polarizabilities

With its access to polarized photon beams and targets, the A2 collaboration at MAMI has undertaken an extensive program to investigate the proton polarizabilities. The present PDG [1] values for the proton scalar polarizabilities are

$$\alpha_{E1}^p = 11.2 \pm 0.4 \times 10^{-4}\,\text{fm}^3 \qquad \beta_{M1}^p = 2.5 \pm 0.4 \times 10^{-4}\,\text{fm}^3. \quad (3)$$

While the errors are not unreasonable, these numbers are from an averaging of various experimental results, and have been reviewed and updated recently without the inclusion of new data. As such, there was a desire to acquire newer data [2]. To extract the scalar polarizabilities, approximately 1000 hours of beam were dedicated to measuring both the unpolarized differential cross section $d\sigma/d\Omega$ and the beam asymmetry Σ_3 below pion production threshold. The analysis of these data is nearing completion, and show unprecedented precision from a single experiment, itself at roughly the precision of the PDG [1] averages.

The spin polarizabilities, on the other hand, had previously only been determined in various linear combinations. To extract the spin polarizabilities, approximately 1250 hours of beam were dedicated to measuring two double polarized observables, Σ_{2x} [3] and Σ_{2z} [4], as well as the beam asymmetry Σ_3, though in this case just below the double pion production threshold. The analyses of these data are complete, and the first two published, which gave (and later improve upon) the first extraction of the individual spin polarizabilities from data.

1.2 Neutron Polarizabilities

While there are still plans to improve upon the proton (mainly spin) polarizabilites, the focus of this proposal is on contributing to the neutron polarizabilities. Investigating these terms are obviously more difficult primarily due to the lack of a free neutron target. As such, the errors on the current PDG [1] numbers

$$\alpha^n_{E1} = 11.8 \pm 1.1 \times 10^{-4}\,\mathrm{fm}^3 \qquad \beta^n_{M1} = 3.7 \pm 1.2 \times 10^{-4}\,\mathrm{fm}^3, \tag{4}$$

are three times larger than those for the proton. These numbers are again averages of a number of experimental efforts to study the neutron, outlined below.

1.2.1 Low-Energy Neutron Scattering

An obvious choice to study the neutron, for which there is no free target, is to instead use it as the beam. By scattering low-energy ($k < 100$ keV) neutrons in the Coulomb field of a heavy nucleus like lead, the cross section can be expanded as:

$$\sigma_s(k) = \sigma_s(0) + ak + bk^2 + \mathcal{O}(k^4) \tag{5}$$

where a depends on α^n_{E1}. Unfortunately, not only did the data from such measurements yield ambiguous results with large errors, from $(12.0 \pm 1.5 \pm 2.0)$ [5] to (0 ± 5) [6] to $(7 - 19)$ [7], all in units of $10^{-4}\,\mathrm{fm}^3$, they also gave no information on β^n_{M1}.

1.2.2 Quasi-free Compton Scattering from Deuterium

The next obvious choice for studying the electromagnetic interaction with a neutron is to look at quasi-free Compton scattering off of the neutron in deuterium. In certain kinematic regions the proton will act only as a spectator, and at low energies the model dependence and nuclear effects are expected to be minimized. An analysis by M. Schumacher in 2005 [8], using the theory of Levchuk and L'vov [9], of data from Saskatoon and Mainz, led to the most precise results at the time of $\alpha^n_{E1} = 12.5 \pm 1.8_{\mathrm{stat}} \pm 1.1_{\mathrm{mod}}$ and $\beta^n_{M1} = 2.7 \mp 1.8_{\mathrm{stat}} \pm 1.1_{\mathrm{mod}}$, both in units of $10^{-4}\,\mathrm{fm}^3$.

1.2.3 Elastic Compton Scattering from Deuterium

Instead of relying on the quasi-free neutron, one can also study elastic Compton scattering from the deuteron as a whole. While the interference between the proton and neutron increases the sensitivity to the polarizabilities, the nuclear effects must be properly taken into account. Recent data from MAX-Lab in Lund [10] improved upon the previous data from Illinois [11], SAL [12], and again from MAX-Lab [13], as shown in Fig. 1.

These data are now the driving force behind the current PDG [1] numbers. In total however, these data are comprised of only 52 points, with clear gaps at some angles and a lack of points at energies close to and above the pion production threshold. Additionally, the relative errors, combining statistical and pt-to-pt systematic errors, range from 7-19% for the recent Lund data [10].

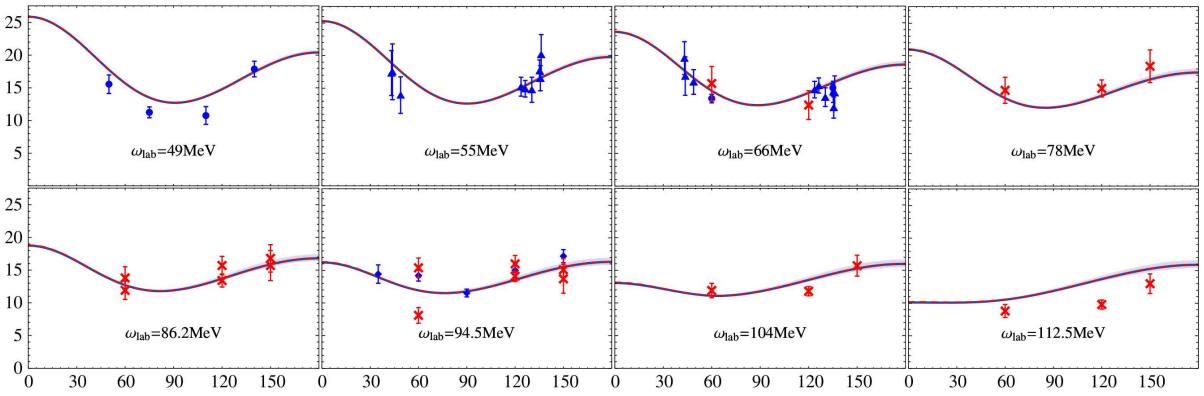

Figure 1: Published data for elastic Compton scattering off of deuterium. The axes are lab differential cross section, in nb/sr, as a function of lab scattering angle, in deg. Figure taken from Myers *et al.* [10], whose data are the red crosses. Additional data are the blue circles from Illinois [11], diamonds from SAL [12], and triangles from MAX-Lab [13].

1.2.4 Elastic Compton Scattering from Helium

As theorists push calculations to larger nuclei, the clear next step is to measure elastic Compton scattering off of helium. While no Compton scattering data exist on ^{3}He, a number of measurements on ^{4}He have been performed, but not significantly in this energy region of interest. There are only 13 published data points between 60 and 90 MeV, with another two points unpublished except for in a thesis from Illinois, as shown in Fig. 2.

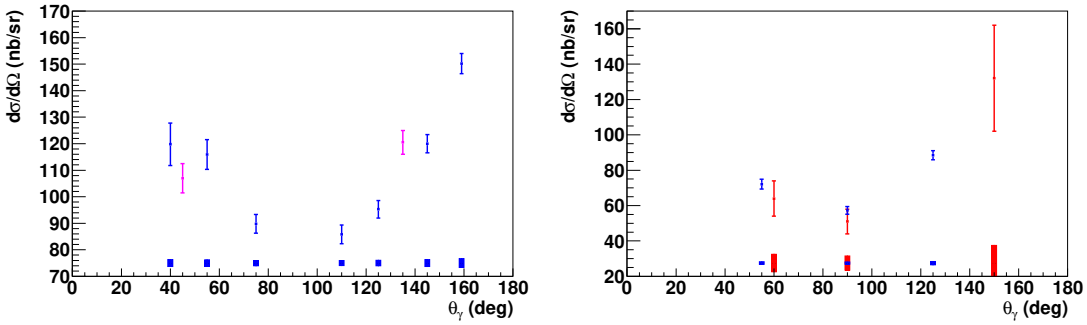

Figure 2: Differential cross sections for Compton scattering off of ^{4}He at 60 MeV (left) and 80 MeV (right). In magenta are two unpublished points from Illinois [14], in red are the published data from Lund [15], and in blue are the published data from HIγS [16,17], the latter two of which depict their correlated systematic errors as bands just above the x-axis.

While a theoretical calculation, as discussed in the next section, is available for ^{3}He (of which there is no data presently) a similar calculation for ^{4}He, which will allow for an extraction from these data, is expected within the next two years. Even more so than in the deuterium case, the number of points is lacking, and the relative errors, combining statistical and pt-to-pt systematic errors, range from 2.5-6.6% for the HIγS data [16,17].

1.3 Chiral Effective Field Theory

Chiral Effective Field Theory (χEFT) predicts that small proton-neutron differences stem from chiral-symmetry breaking interactions of the pion cloud around the nucleon and therefore probe the symmetries of QCD directly. However, as shown, neutron information to date is quite limited. Experimentally the target neutron must be bound in a light nucleus, which complicates the polarizability analysis. On the other hand, this provides the opportunity to couple to the charged meson-exchange currents which bind the nucleus together. Around pion-production threshold, one can also study the transition to a dynamical Δ, to understand better its role not only for nucleons, but also for the few-body nuclei. New experiments on light nuclei are needed to determine specific polarizabilities and test our understanding of strong and photonuclear interactions on the hadronic scale.

Over the last few decades there has been significant work in χEFT, dispersion relations, quark models, and lattice QCD. Calculations within χEFT exist for a variety of polarized and unpolarized observables for protons and deuterons [18], as well as ^{3}He [19]. The first is being used in the recent efforts at A2 for studying the proton scalar polarizabilities [2], and the second was used above for the neutron scalar polarizabilities [10]. The third is an improved version of Shukla *et al.* [20], having been extended to $\mathcal{O}(e^2\delta^3)$ with the explicit inclusion of the $\Delta(1232)$. Calculations within this framework are shown in Fig. 3, demonstrating the affects that the proton and neutron polarizabilities play in ^{3}He.

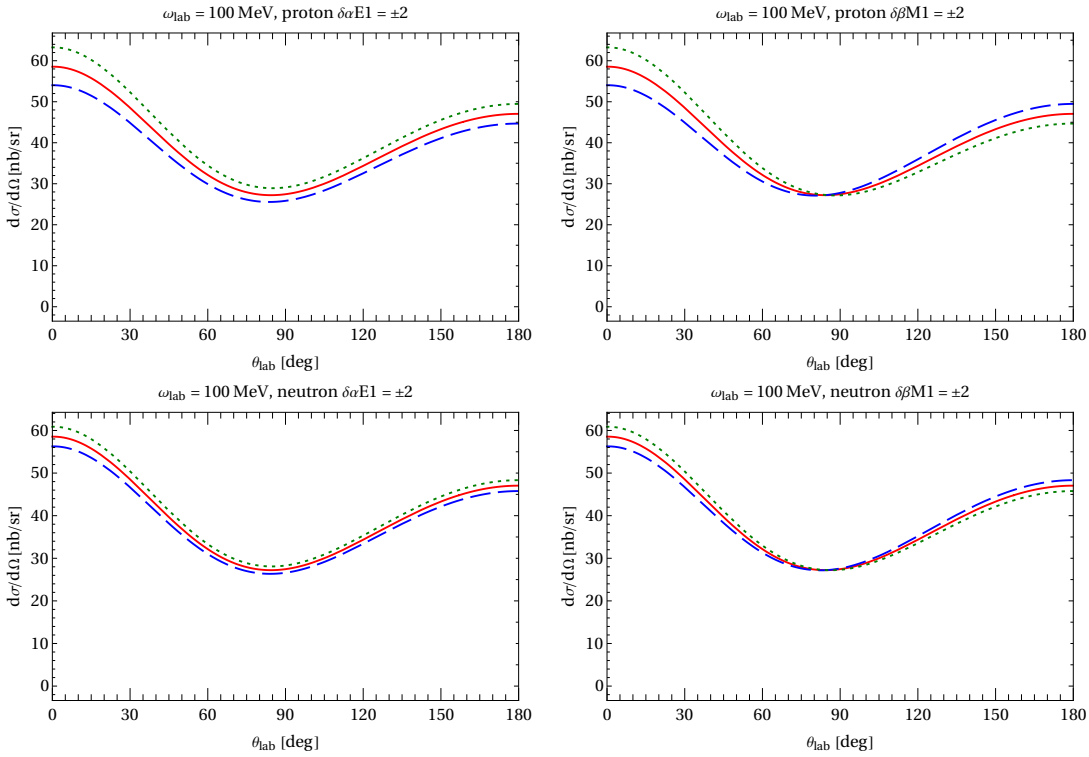

Figure 3: Unpolarized differential cross section calculations within χEFT for Compton scattering off of ^{3}He [19] for $E_\gamma = 100$ MeV as functions of lab scattering angle. The solid red curve is the result using present PDG values, with the dotted green and dashed blue representing a change to the proton (top) or neutron (bottom), electric (left) or magnetic (right), polarizability of ± 2. Produced in a Mathematica notebook provided by H.W. Grießhammer.

Helium isotopes ($Z = 2$) have a significantly larger Compton scattering cross section than the deuteron ($Z = 1$) and at 120 MeV the cross section scales as $\sim Z$. In helium, interference of the proton Thomson terms with the neutron polarizability amplitudes produces a greater sensitivity of the differential cross section to the polarizabilities. ^{4}He is both a scalar and isoscalar target, offering the potential for complementary polarizability information, and it will also provide important checks on the accuracy of the theoretical treatment of nuclear binding and meson-exchange currents. Ultimately a polarized ^{3}He (effectively a polarised neutron target) experiment would provide access to the neutron spin polarizabilities. However, before this stage is reached, it is important to test χEFT predictions of the ^{3}He differential cross section which are relatively undeveloped due to a complete lack of data. New data on ^{4}He will provide a more exacting test of χEFT predictions and also an alternative proton-neutron 'mix' of the isospin averaged polarizabilities.

2 Proposed Experiments

With the presently available data as well as the χEFT calculations in mind, there is clearly a need for Compton scattering data on deuterium as well as on both ^{3}He and ^{4}He. As such, we propose a combined effort to measure two of these, and push towards measuring the third. These experiments will take place in the A2 hall at MAMI, making use of the tagged Bremsstrahlung beam discussed in Sec. A.1 incident upon targets discussed below, with the final state particles detected in the combined CB/TAPS detector system discussed in Secs. A.4 and A.5.

2.1 Compton Scattering off of Deuterium

As in the A2 program for extracting the proton scalar polarizabilities, the proposed neutron program relies upon precise measurements of the Compton scattering differential cross section below pion production threshold. In the proton program, the target was a cell of liquid hydrogen (see Sec. A.2), from which the only backgrounds below pion production are from the target windows, a contribution that can be subtracted with separate empty-target runs. While such backgrounds with the liquid deuterium target, which is the same cryostat, will be dealt with in a similar fashion, there are additional backgrounds to consider.

Elastic Compton scattering off of ^{2}H, $\gamma + {}^2\mathrm{H} \to \gamma + {}^2\mathrm{H}$, has the following background reactions:

- $\gamma + {}^2\mathrm{H} \to \gamma + p + n$ (quasi-free)
- $\gamma + {}^2\mathrm{H} \to p + n$ (breakup)

The energy resolution of the CB is unfortunately not sufficient to directly separate the coherent from the quasi-free process, as the binding energy of deuterium is only 2.2 MeV. Below pion production, the detection of a residual final-state proton is not possible due to energy losses in reaching the detectors. The detection of a residual final-state neutron is possible, but not for all kinematics. An active deuterated target could be utilized to tag the quasi-free proton, with the caveat that this would introduce a large background from coherent and incoherent scattering off of carbon. A future solution for this problem

was found in discussions with our theory colleagues. They are already in the process of developing a combined coherent and quasi-free χEFT calculation, allowing for the extraction of the polarizabilities from the unseparated cross section. With this process already underway, expanding the database of Compton scattering off of deuterium with more angular points and to higher energies is a worthwhile endeavor. Therefore we propose to measure the unpolarized differential cross section for Compton scattering off of deuterium from 65 MeV to pion threshold. We will also measure from pion threshold up to 200 MeV, or as close as is permitted when relying upon simulation to reject pion backgrounds.

2.2 Compton Scattering off of Helium

Similar to the deuteron case, there are additional backgrounds that must be considered for Compton scattering off of helium. Elastic Compton scattering off of ^{3}He, $\gamma + {}^3\text{He} \rightarrow \gamma + {}^3\text{He}$, has the following background reactions:

- $\gamma + {}^3\text{He} \rightarrow \gamma + p + {}^2\text{H}$ (quasi-free)
- $\gamma + {}^3\text{He} \rightarrow p + {}^2\text{H}$ (breakup)
- $\gamma + {}^3\text{He} \rightarrow p + p + n$ (breakup)

The energy resolution of the CB is also not sufficient to directly separate the coherent from the quasi-free process, as the change in binding energy between ^{3}He and deuterium is only 4.5 MeV. Like the deuteron case, a combined coherent and quasi-free χEFT calculation would be possible, but unlike the deuteron case, it is not presently being developed and would require a non-insignificant effort by our theory colleagues. As such an effort is not envisioned here in the short term, a way of experimentally separating these reactions would be needed, and will be discussed in Sec. 2.4.

Elastic Compton scattering off of ^{4}He, $\gamma + {}^4\text{He} \rightarrow \gamma + {}^4\text{He}$, has the following background reactions:

- $\gamma + {}^4\text{He} \rightarrow \gamma + p + {}^3\text{H}$ (quasi-free)
- $\gamma + {}^4\text{He} \rightarrow \gamma + n + {}^3\text{He}$ (quasi-free)
- $\gamma + {}^4\text{He} \rightarrow p + {}^3\text{H}$ (breakup)
- $\gamma + {}^4\text{He} \rightarrow n + {}^3\text{He}$ (breakup)
- $\gamma + {}^4\text{He} \rightarrow p + n + {}^2\text{H}$ (breakup)
- $\gamma + {}^4\text{He} \rightarrow p + p + n + n$ (breakup)
- $\gamma + {}^4\text{He} \rightarrow {}^2\text{H} + {}^2\text{H}$ (breakup)

While there are many more background reactions, in this case the energy resolution of the CB is sufficient to directly separate the coherent from the quasi-free processes, as the change in binding energy between ^{4}He and ^{3}H is 19.8 MeV and between ^{4}He and ^{3}He is 21.1 MeV.

2.3 Liquid Helium Target

The liquid helium target in the A2 hall is similar in concept to the liquid deuterium target. The target cell is a Mylar cylinder with a length of 5 cm and diameter of 3 cm. At temperatures of 2.15 K, the target density is 126 kg/m^3 [21]. A schematic of the target is shown in Fig. 4.

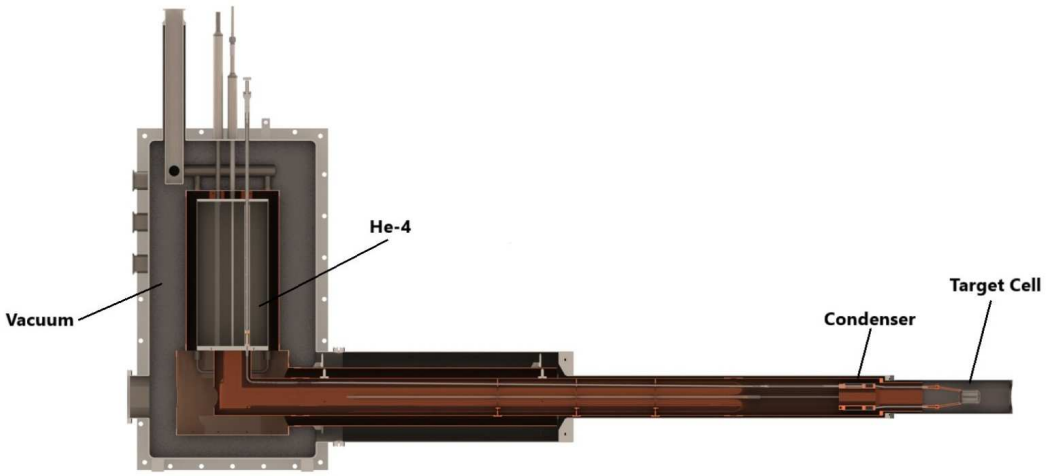

Figure 4: Liquid helium target schematic [21].

2.4 Active Helium Target

To allow for identification of the non-elastic reactions on helium, critical for ^{3}He, an active target is envisioned. Helium naturally scintillates during the passage of a charged particle. Detecting this scintillation light with sufficient energy resolution would enable a separation of a recoiling deuteron ion from a quasi-free proton. An active high-pressure gas target had been built for such a purpose at MAX-Lab, and was transferred to Mainz with the intention of modifying it such that it would function within the CB. Due to difficulties in this modification, and concerns over the pressures anticipated, a design for a new target was drafted, as shown in Fig. 5.

The vessel is a simple cylinder with a sheet of PTFE around the inside surface in which a matrix of 6x6 mm SiPMs are installed. These SiPMs are the same as used in the upgraded tagger system in A2, described in Sec. A.1. A half-length prototype has been constructed, and initial tests performed. These tests unfortunately indicated that the light collection on each detector was insufficient to overcome the electronic noise unless the scintillation event is very close to the detector face. One possible solution being examined is the use of wavelength shifting fibers. Helium scintillates in the VUV (Vacuum Ultraviolet), wavelengths far shorter than the absorption of traditional detectors. To compensate for this, a small amount of nitrogen is added to the helium gas to shift the wavelength. Another option for a VUV wavelength shifter is Tetraphenyl-Butadiene (TPB), which St. Gobain can dope in polystyrene and produce wavelength shifting fibers. Covering the inner surface of the vessel with these fibers, wrapped either helically or longitudinally, would provide a larger surface area for light collection, which could then

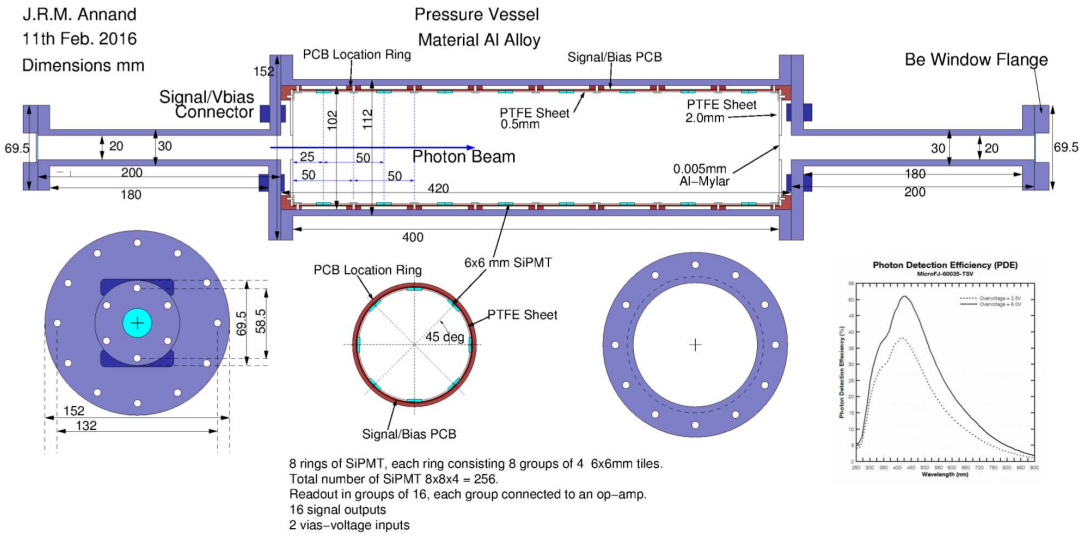

Figure 5: Active target schematic.

be shifted and propagated down the fiber to the SiPMs. Feasibility studies on this will continue this summer.

2.5 Compact TPC with CB

Another possibility for the identification of these non-elastic reactions on helium, again critical for ^{3}He, comes in the form of a compact TPC in place of the active target. This will be described in a separate letter of intent, and as such will not be discussed further here.

2.6 Helium Proposal

Although measurements of Compton scattering off of ^{3}He are crucial, and will certainly be taken at some point, there is further work needed on either the experimental side with an 'active' target or on the theoretical side with a combined coherent and quasi-free χEFT calculation for ^{3}He. Efforts will continue on the target side in A2, but in the meantime a significant improvement can be made on the data for ^{4}He with the presently available liquid helium target described above. Therefore we propose to measure the unpolarized differential cross section for Compton scattering off of ^{4}He from 65 MeV to pion threshold. We will also measure from pion threshold up to 200 MeV, or as close as is permitted when relying upon simulation to reject pion backgrounds.

3 Recent MAMI Data on Helium

A test run of 125 hours was taken with the liquid ^{4}He target in June 2019. Elastic Compton scattering cross sections will be obtained from these data beginning at 65 MeV and going at least up to pion threshold, and as far beyond as agreement with simulation will allow. A preliminary example of this data at 80 MeV is shown in Fig. 6, compared with the previously published data shown in Fig. 2.

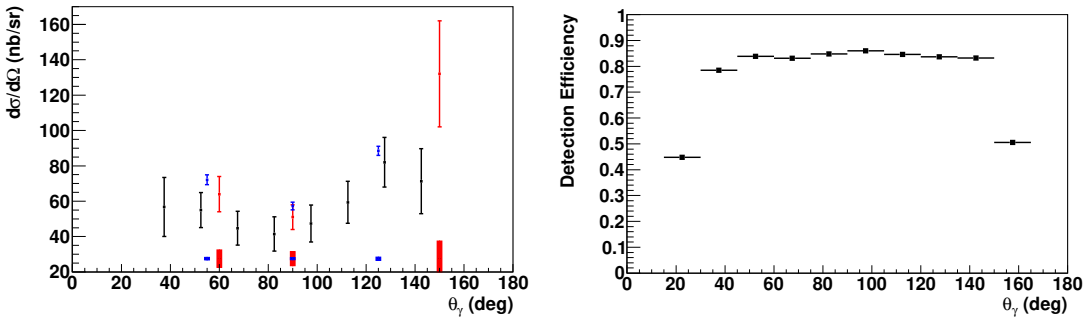

Figure 6: (Left) Differential cross sections for Compton scattering off of ^{4}He at 80 MeV. In black are the recent preliminary data taken at MAMI, in red are those from Lund, and in blue are those from HIγS, the latter two of which depict their correlated systematic errors as bands just above the x-axis. (Right) Detection efficiency for this analysis for the MAMI data at 80 MeV.

While the preliminary error bars are larger with this new data, this test run served as confirmation of the ability to resolve the elastic peak from the quasi-free and breakup processes in ^{4}He. Both of the proposed experiments detailed in the following two sections utilize the lessons learned from this test in order to give reasonable estimates for total yields and uncertainties. The two major improvements will be running at a MAMI energy of 883 MeV, as opposed to 450 MeV as used in the test run, and using the diamond radiator to produce linearly polarized photons with a coherent edge at $\approx$ 145 MeV. While the goal of both experiments is to measure the unpolarized differential cross section, the use of linear polarization leads to a significant increase in the tagging efficiency which is the ratio of photons on target versus those produced. In order to ensure the photon beam remains on target, a collimator with a diameter of 2.5 mm is used. As shown in Tab. 4, the tagging efficiency for the 450 MeV test run was therefore $\approx$ 8.3%, while for unpolarized 883 MeV it would be $\approx$ 25.7%. This can be compared with the case for a linearly polarized beam and a coherent edge of $\approx$ 145 MeV, as shown on the left of Fig. 7.

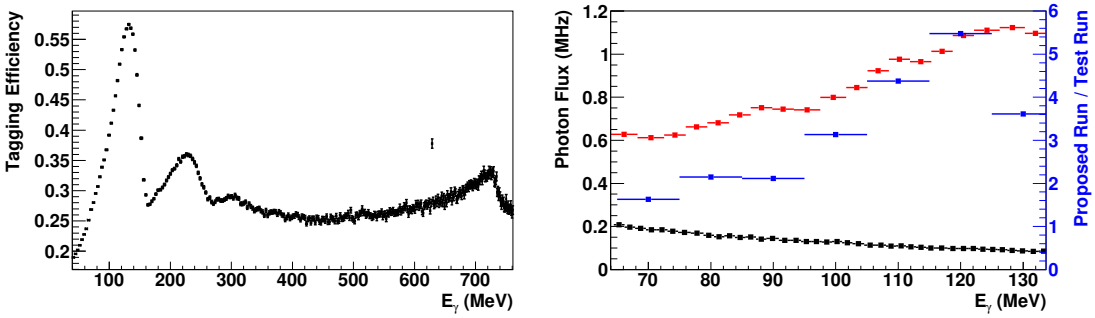

Figure 7: (Left) Tagging efficiency for linearly polarized photons from a MAMI beam of 883 MeV, using a coherent edge of $\approx$ 145 MeV. (Right) Photon flux rate over the energy range of interest is shown in black for unpolarized 450 MeV and in read for linearly polarized 883 MeV, both normalized such that the first channel has an electron flux of 2.5 MHz, with the ratio of the integrated flux within 10 MeV bins between these two shown in blue.

The large first peak begins descending around $\approx$ 135 MeV, with the half-max of the

falloff denoting the coherent edge of $\approx$ 145 MeV. The right hand plot then compares the photon flux rate obtained in the 450 MeV test run to that using linear polarization at 883 MeV, where they have both been normalized such that the first channel is at the prescribed tagger limit of 2.5 MHz. It should be noted that running at this higher energy increases the single tagger channel bin width by a factor of two. This change is permissible, given desired energy widths for the cross section data of $\approx$ 10 MeV still correspond to more than one channel, but must be accounted for in the resulting increase in photon flux. The blue points show the ratio of the integral of each of these fluxes over a 10 MeV bin. The points at 90 and 130 MeV are lower than expected due to these bins integrating only two of the 883 MeV bins, instead of three as in the others. This denotes a photon flux rate of 2, 3, and 5.5 times that of the test run for 80, 100, and 120 MeV, respectively. These photon flux rates will be used in the following sections.

4 Cross Sections and Projected Data

For both experiments the detection efficiencies given in Fig. 6 as well as the photon flux rates given in Fig. 7 were used to estimate the count rates and resulting errors. In addition to the statistical error from the pure counts, the statistical error with random coincidence and empty target backgrounds is estimated based on the liquid ^{4}He test run. The determination of the incident photon energy relies on a timing correlated (prompt) hit in the tagger with respect to the final state particles detected in the CB/TAPS systems. As the rate in the tagger increases, the background of random coincidences under this prompt timing peak increases quadratically. The ratio of the random coincidences to prompt correlations, R/P, scales the resulting statistical error by a factor of $\sqrt{1+R/P}$. The other effect is beam related background from the windows of the target cryostat. This background is subtracted out by taking an appropriate amount of data with the target in an empty state. Assuming an absolute error on the empty target yield of an equal size to the full target yield, also accounting for the previous random coincidence background, the extracted 'statistical' error is scaled by an additional factor of $\sqrt{2}$.

4.1 Compton Scattering off of Deuterium

The calculations for the count rates and resulting errors for deuterium all use a density of 0.16324 g/cm^3 and a target length of 10 cm, giving a total number of target nuclei of 4.915×10^{23}. With 200 hours of running time the expected data with errors are shown in Fig. 8, along with a sample at $\theta_\gamma = 82.5 \pm 7.5$ deg ($\Omega = 1.626$ sr) tabulated in Tab. 1. The scaled statistical errors vary from 3.8-6.1%, a marked improvement over currently published data.

4.2 Compton Scattering off of Helium

The calculations for the count rates and resulting errors for ^{4}He all use a density of 0.126 g/cm^3 and a target length of 5 cm, giving a total number of target nuclei of 9.484×10^{22}. With 300 hours of running time the expected data with errors are shown in Fig. 9, along with a sample at $\theta_\gamma = 82.5 \pm 7.5$ deg ($\Omega = 1.626$ sr) tabulated in Tab. 2. The scaled statistical errors vary from 4.7-6.3%, again a marked improvement over currently published data, especially as it extends to higher energies than previously measured.

E_γ (MeV)	$d\sigma/d\Omega$ (nb/sr)	F_γ (MHz)	R/P	$\epsilon_{\rm det}$	N	σ/N (%)	$\sigma^{'}/N$ (%)
80	12.05	2.06	16.1	0.85	12127	0.91	5.31
100	11.55	2.39	15.5	0.90	14215	0.84	4.82
120	11.75	3.21	13.8	0.89	19223	0.72	3.92

Table 1: Projected data points for elastic Compton scattering off of deuterium at $\theta_\gamma = 82.5 \pm 7.5$ deg and incident photon energies $E_\gamma = 80$, 100, and 120 MeV (each ± 5 MeV) with 200 hours of running. $d\sigma/d\Omega$ is the cross section calculated in a Mathematica notebook provided by H.W. Grießhammer [18]. For each energy bin: F_γ is the photon flux rate, R/P is the ratio of random coincidences to prompt timing correlations, and $\epsilon_{\rm det}$ is the detection efficiency. From these, and the number of nucleons and solid angle given in the text, the number of counts N after 200 hours of running is determined, along with its relative statistical error σ/N. This is then scaled, based on R/P and an equal error from the empty target, to give the extracted 'statistical' error $\sigma^{'}/N$.

E_γ (MeV)	$d\sigma/d\Omega$ (nb/sr)	F_γ (MHz)	R/P	$\epsilon_{\rm det}$	N	σ/N (%)	$\sigma^{'}/N$ (%)
80	44.67	2.06	16.1	0.85	13014	0.88	5.13
100	32.86	2.39	15.5	0.90	11707	0.92	5.31
120	22.67	3.21	13.8	0.89	10734	0.97	5.25

Table 2: Projected data points for elastic Compton scattering off of ^{4}He at $\theta_\gamma = 82.5 \pm 7.5$ deg and incident photon energies $E_\gamma = 80$, 100, and 120 MeV (each ± 5 MeV) with 300 hours of running. $d\sigma/d\Omega$ is the cross section for ^{3}He calculated in a Mathematica notebook provided by H.W. Grießhammer [19], and scaled by a factor of 1.2 to roughly match the data from the test run on ^{4}He. Otherwise similar to Tab. 1.

4.3 Overview of Requested Beamtime

The summary of this beamtime request is given in Tab. 3. With the statistics acquired in the proposed Compton scattering program, the A2 collaboration at MAMI would provide a deuterium dataset of improved accuracy and at energies and angles not before measured, and a ^{4}He dataset of similar accuracy to the best published data but especially at a number of energies and angles not before measured. Such a database will permit the extraction of the neutron scalar polarizabilities with unmatched precision.

Task	LD2 Time (hours)	LHe Time (hours)
Setup	10	10
Tagging Efficiency	40	80
Full Target Running	200	300
Empty Target Running	100	260
Subtotal	**350**	**650**
Total	**1000**	

Table 3: Requested beamtime for this proposal.

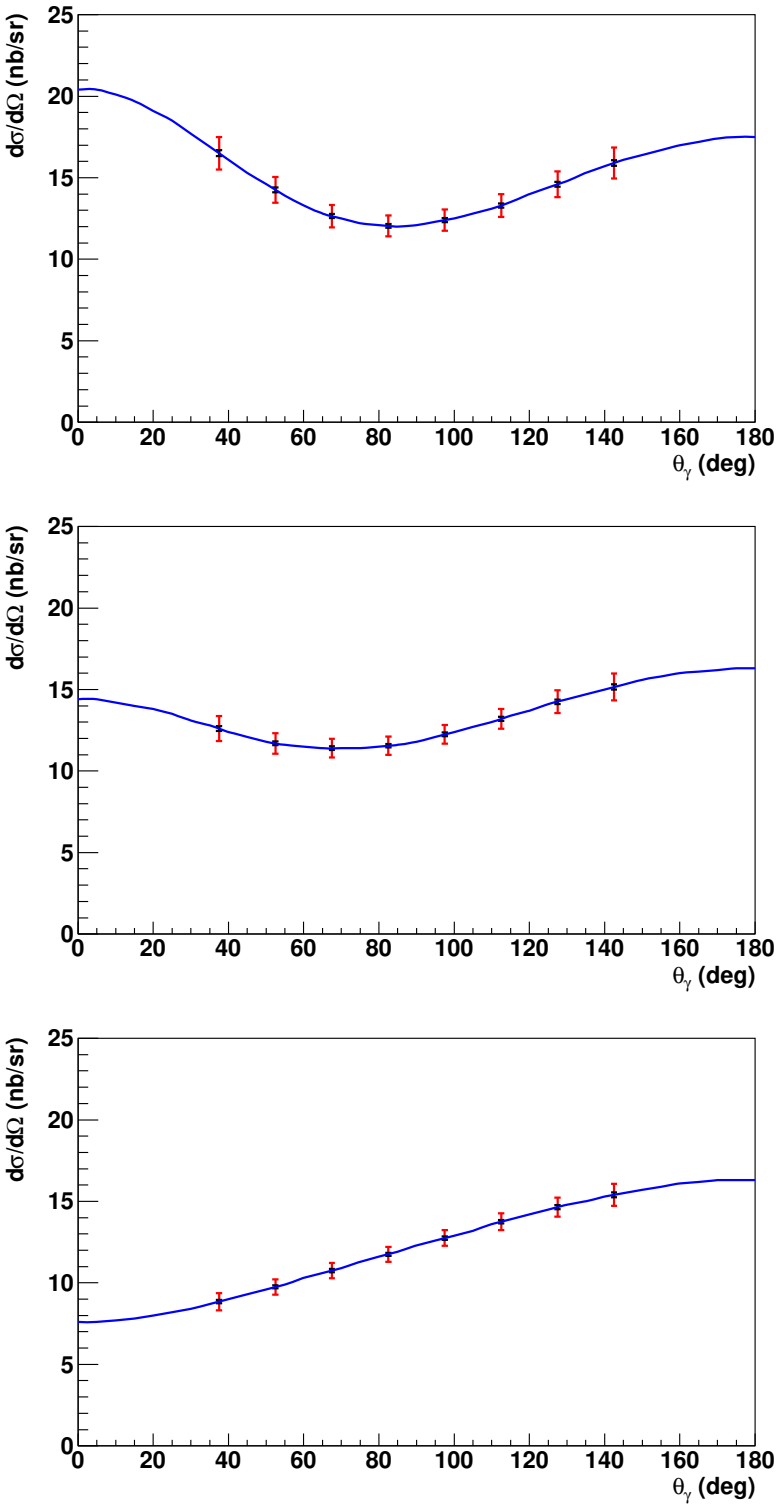

Figure 8: Projected data points for elastic Compton scattering off of deuterium with 200 hours of running. From top to bottom are incident photon energies of 80, 100, and 120 MeV, each ±5 MeV. The black bars denote the purely statistical error assuming no random coincidence or empty target backgrounds. The red bars denote the expectation given backgrounds equivalent to the test run on liquid helium. The blue lines are the χEFT calculations for deuterium.

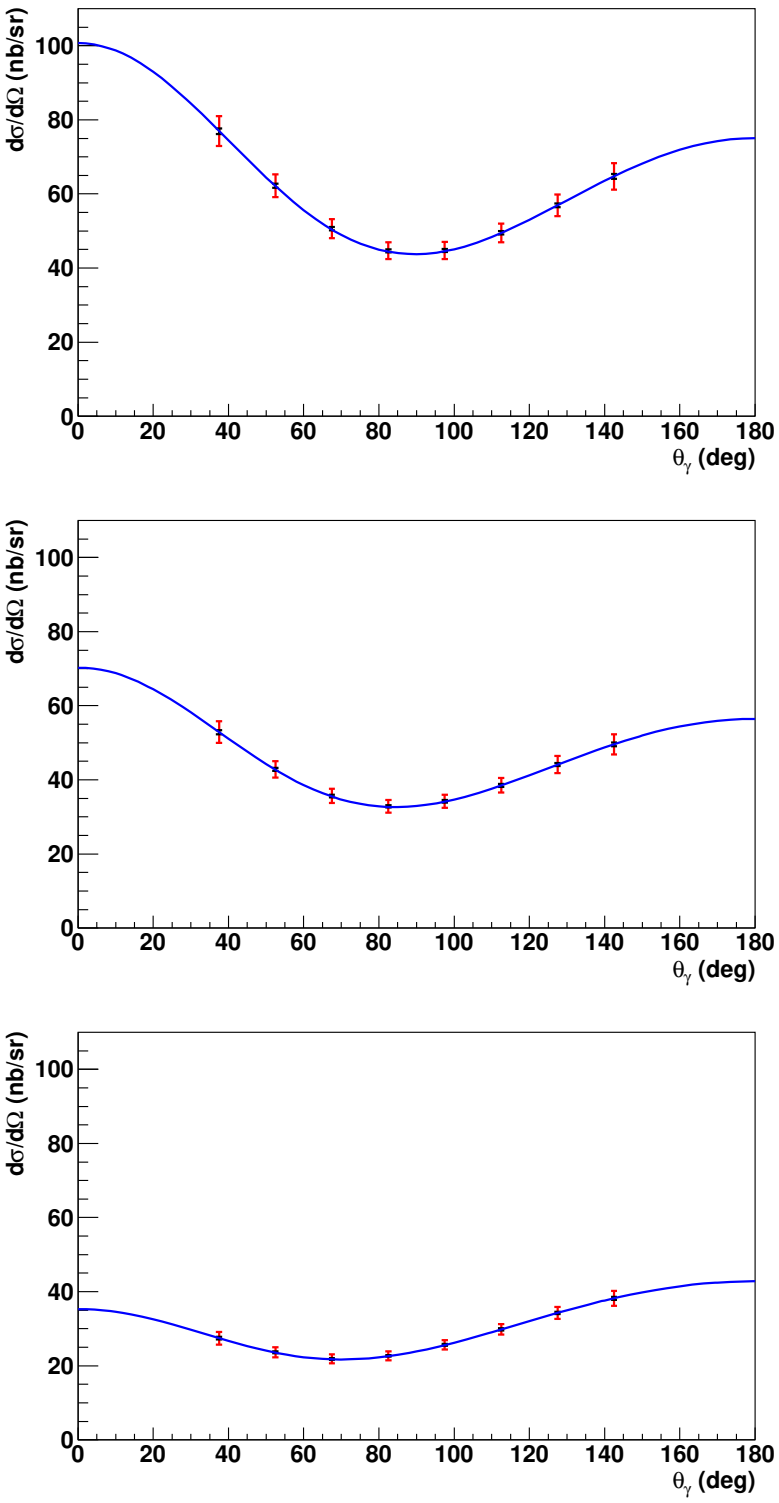

Figure 9: Projected data points for elastic Compton scattering off of ^{4}He with 300 hours of running. From top to bottom are incident photon energies of 80, 100, and 120 MeV, each $\pm$5 MeV. The black bars denote the purely statistical error assuming no random coincidence or empty target backgrounds. The red bars denote the expectation given backgrounds equivalent to the test run on liquid helium. The blue lines are the χEFT calculations for ^{3}He scaled by a factor of 1.2.

A Experimental apparatus

A.1 Photon Beam

The A2 photon beam is derived from the production of Bremsstrahlung photons during the passage of the MAMI electron beam through a thin radiator. The resulting photons can be circularly polarised, with the application of a polarised electron beam, or linearly polarised, in the case of a crystalline radiator. The degree of polarisation achieved is dependent on the energy of the incident electron beam (E_0), the energy range of interest, and in the case of linear polarisation on the photon collimator size. Together, these currently result in a peak of ∼75% for linear polarisation (Fig. 10) and ∼85% for circular polarisation (Fig. 11). The collimator size, as well as the electron beam energy, also affect the ratio of photons that reach the target to those produced in the Bremsstrahlung process. Typical values for this ratio, denoted as the tagging efficiency, are shown in Tab. 4. The upgraded A2 Photon Tagger (Fig. 12) provides energy tagging of the photons by detecting the post-radiating electrons with a single-counter time resolution $\sigma_t = 0.1$ ns [22]. With the upgrade, individual counters can now operate reliably above 1 MHz, although the loss due to pile-up is ∼1.8% per 1 MHz rate. A typical limit of 2.5 MHz is employed to keep the pile-up loss below 5%. Photons can be tagged in the momentum range from 4.3 to 93.0% of E_0, with resolutions varying from 0.4 to 0.05% of E_0, respectively. This relationship, along with sample rate distributions, is shown in Fig. 13.

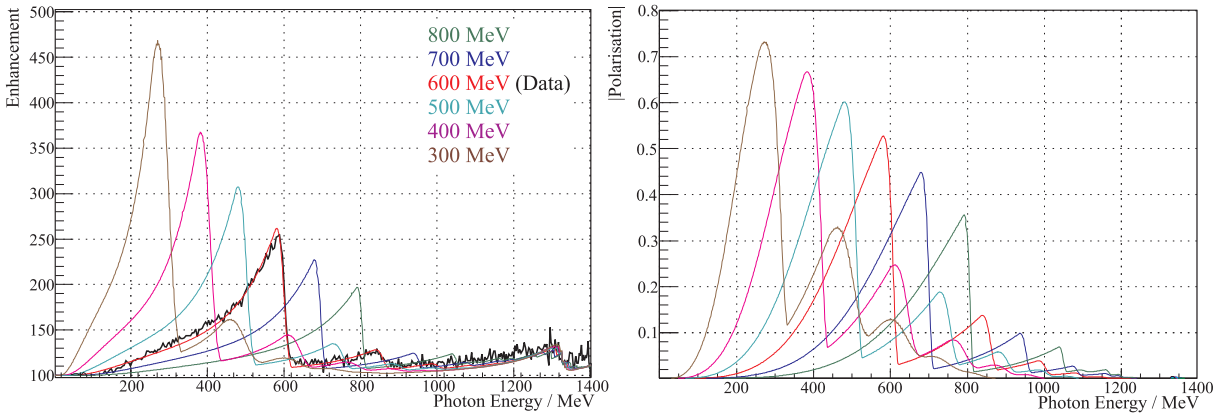

Figure 10: Linear polarisation available with the current collimation system for a variety of crystal orientations. The thin black lines are data obtained during MAMI runs.

E_0 (↓) / d_{col} (→)	1.5 mm	2.0 mm	2.5 mm	3.0 mm	4.0 mm
180 MeV	0.54	1.0	1.6	2.3	4.2
450 MeV	3.2	5.4	8.3	12.1	19.5
883 MeV	9.9	17.7	25.7	33.1	44.4
1557 MeV	16.0	27.0	37.8	49.0	66.5

Table 4: Tagging efficiencies, in %, for typical incoming electron beam energies (E_0) and photon collimator diameters (d_{col}).

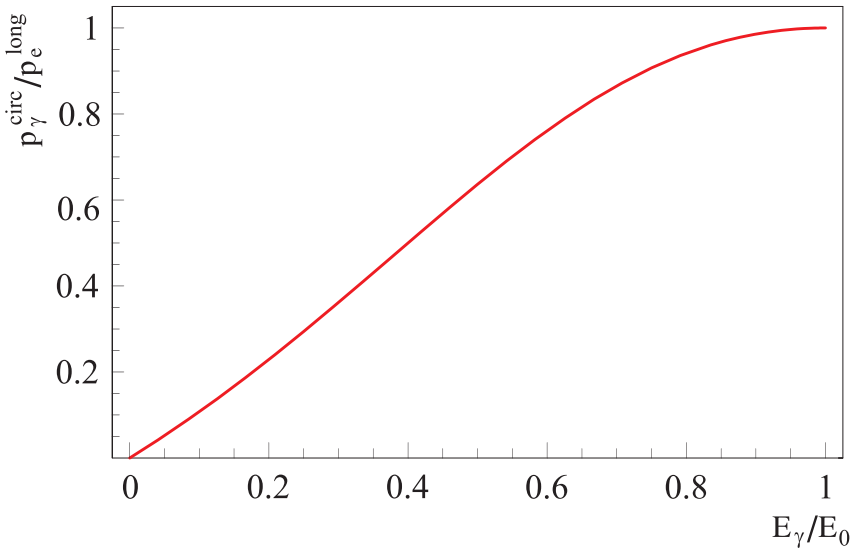

Figure 11: Helicity transfer from the electron to the photon beam as function of the energy transfer. The MAMI beam polarisation is $P_e \approx 85\%$.

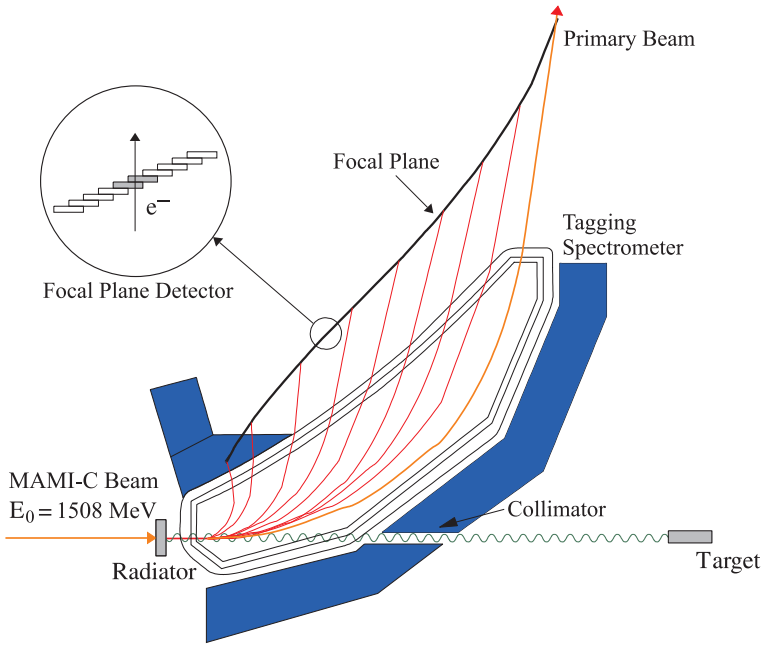

Figure 12: The Glasgow-Mainz photon tagging spectrometer.

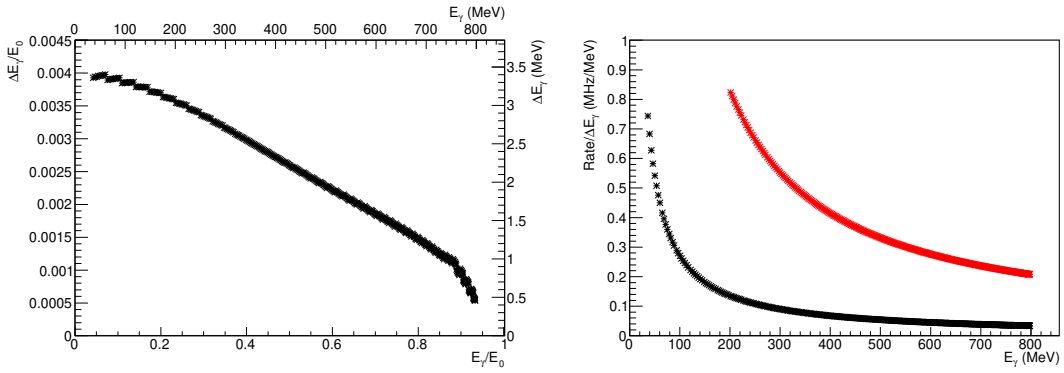

Figure 13: (Left) Tagger channel width (resolution) as a function of the tagged photon energy. The left and bottom axes show these values as relative to the incoming electron beam energy. The right and top axes show these values for a standard electron beam energy of 855 MeV. (Right) Rates in MHz per MeV for a beam energy of 855 MeV, assuming a $1/E_\gamma$ Bremsstrahlung distribution, if the first channel is run at 2.5 MHz (black) or if the first 48 channels are switched off and the next is run at 2.5 MHz (red).

A.2 Liquid Hydrogen (Deuterium) Target

The Hydrogen (Deuterium) target apparatus uses a cold head to liquify the target gas from a 2 m^3 storage container into a cylindrical, thin walled plastic cell at temperatures around $\approx$ 20K ($\approx$ 24K). The pressure of the saturated target liquid is stabilized by a dedicated control system to typically 1080 ± 2 mBar for both isotopes. This leads to a density of 70.548 ± 0.01 kg/m^3 for Hydrogen (163.24 ± 0.02 kg/m^3 for Deuterium). The Hydrogen target was designed to retain the high angular acceptance of the detector system. The acceptance of the hydrogen target is shown in figure 14. This system provides a low material budget in the region between 21° and 159° in the polar angle (θ) and over the full azimuthal (ϕ) range, adapted to our central Crystal Ball detector. At forward angles, less than 21°, where reaction products are detected in the TAPS forward wall, a thin ($\approx$ 2.5 mm) aluminium flange is used with a glued on 125 μm thick Kapton window.

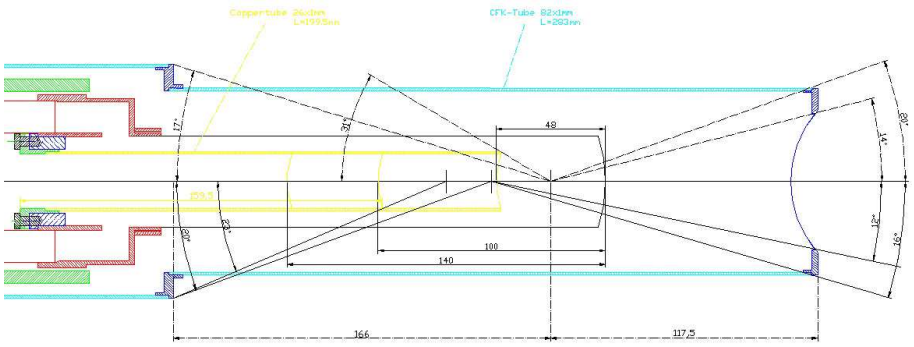

Figure 14: The A2 hydrogen target geometry and acceptance is shown for cell lengths of 48mm and 100mm.

The target length can be changed by using different entrance window adapters to 30.2 ± 0.3 mm, 47.2 ± 0.5 mm or 100.0 ± 1.0 mm. The cell for the target liquid is made of 125 μm Kapton, surrounded by 8 layers of superisolation foil (each 8 μm Mylar + 2 μm

Figure 15: The dilution refrigerator for the Crystal Ball Frozen Spin Target.

Aluminum). A Carbon fibre tube of 82 mm outer diameter and 1 mm wall thickness holds the isolation vacuum.

A.3 Frozen-Spin Target

Polarisation experiments using high density solid-state targets in combination with tagged photon beams can reach the highest luminosities. For the double polarisation measurements planned with the Crystal Ball detector on polarised protons and deuterons a specially designed, large horizontal ^{3}He/^{4}He dilution refrigerator was built in cooperation with the Joint Institute for Nuclear Research (JINR) Dubna (see Fig. 15). It has minimum limitations for the particle detection and fits into the central core of the inner Particle Identification Detector (PID). This was achieved by using the frozen spin technique with the new concept of placing a thin superconducting holding coil inside the polarisation refrigerator. Longitudinal and transverse polarisations will be possible.

Highest nucleon polarisation in solid-state target materials is obtained by a microwave pumping process, known as 'Dynamic Nucleon Polarisation' (DNP). This process is applicable to any nucleus with spin and has already been used in different experiments with polarised proton and deuteron targets. The geometric configuration of the target is the same for the polarised proton and neutron setup. However, since the polarisation measurement of the deuteron is more delicate due to the small size of the polarisation signals, the modification of some basic components is needed. The reason for this is twofold: firstly the magnetic moment of the deuteron is smaller than that of the proton and, in addition, the interaction of the deuteron quadrupole moment with the electric field gra-

dient in the sample broadens the deuteron polarisation signal. An accuracy $\delta P_p/P_p$ of 2 to 3% for the protons and $\delta P_D/P_D$ of 4 to 5% for the deuterons is expected in the polarisation measurement. It has also to be taken into account that the measured deuteron polarisation P_D is not equal to the neutron polarisation P_n. Assuming a 6 % admixture of the D-state of the deuteron, a calculation based on the Clebsch-Gordon coefficients leads to $P_n = 0.91\ P_D$. Several polarised proton and deuteron materials are available such as alcohols and deuterated alcohols (e.g. butanol C_4H_9OH), NH_3, ND_3 or ^{6}LiD. The most important criteria in the choice of material suitable for particle physics experiments are the degree of polarisation P and the ratio k of free polarisable nucleons to the total number of nucleons. Further requirements on polarised target materials are a short polarisation build-up time and a simple, reproducible target preparation. The polarisation resistance against radiation damage is not an issue for experiments with a low intensity tagged photon beam ($\dot{N}_\gamma \approx 5 \cdot 10^7\ \mathrm{s}^{-1}$) as will be used here.

Taking all properties together, butanol and deuterated butanol are the best material for this experiment. For protons we expect a maximum polarisation of $P_p = 90\%$ and an average polarisation of $P_p = 70\%$ in the frozen spin mode. Recently, a deuteron polarisation $P_D = 80\%$ was obtained with Trityl doped butanol targets at 2.5 T magnetic field in a ^{3}He/^{4}He dilution refrigerator. At a 0.4 T holding field an average neutron polarisation P_n (see above) of 50 % will be obtained. The filling factor for the ~ 2 mm diameter butanol spheres into the 2 cm long, 2 cm diameter target container will be around 60%. The experience from the GDH runs in 1998 [23] shows that, with a total tagged photon flux of $5 \cdot 10^7$, relaxation times of about 200 hours can be expected. The polarisation has to be refreshed by microwave pumping every two days.

In conclusion, we estimate that we will achieve the following target parameters:

- Maximum total tagged photon flux in the energy range of 4.7 to 93% of E_0: $\dot{N}_\gamma \approx 5 \cdot 10^7\ \mathrm{s}^{-1}$, with relaxation time of 200 hours.
- Target proton density in 2 cm cell: $N_T \approx 9.1 \cdot 10^{22}\mathrm{cm}^{-2}$ (including dilution and filling factors)
- Average proton polarisation $P_p = 70\%$
- Target deuteron density in 2cm cell: $N_T \approx 9.4 \cdot 10^{22}\mathrm{cm}^{-2}$ (including dilution and filling factors)
- Average neutron polarisation $P_n = 50\%$

A.4 Crystal Ball Detector System

The central detector system consists of the Crystal Ball calorimeter combined with a barrel of scintillation counters for particle identification and two coaxial multiwire proportional counters for charged particle tracking. This central system provides position, energy and timing information for both charged and neutral particles in the region between 21° and 159° in the polar angle (θ) and over almost the full azimuthal (ϕ) range. At forward angles, less than 21°, reaction products are detected in the TAPS forward wall. The full, almost hermetic, detector system is shown schematically in Fig. 16 and the measured two-photon invariant mass spectrum is shown in Fig. 17.

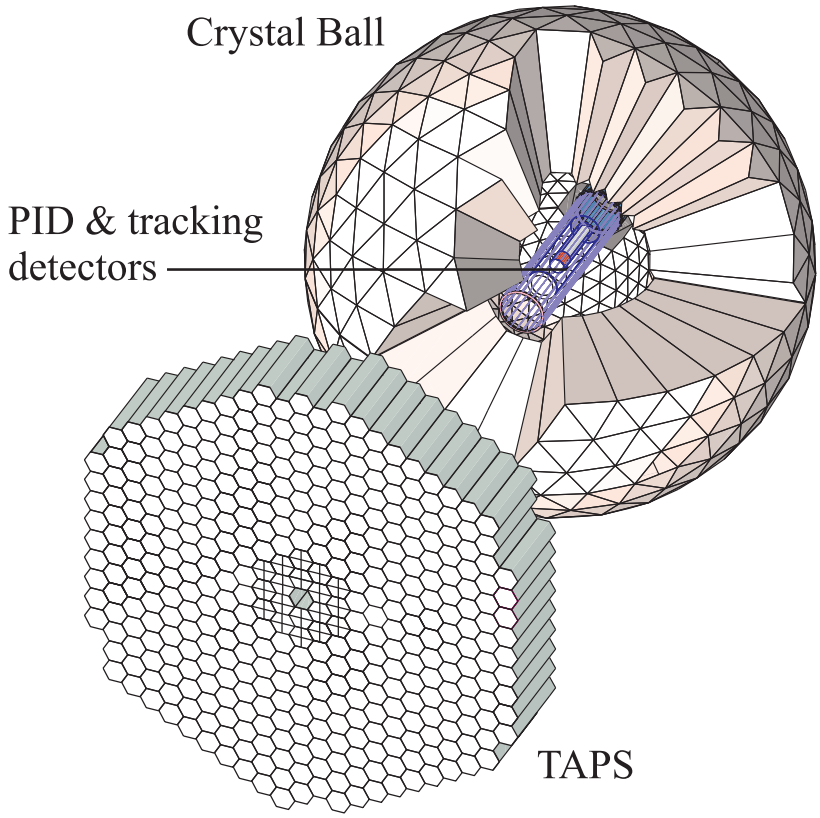

Figure 16: The A2 detector setup: The Crystal Ball calorimeter, with cut-away section showing the inner detectors, and the TAPS forward wall.

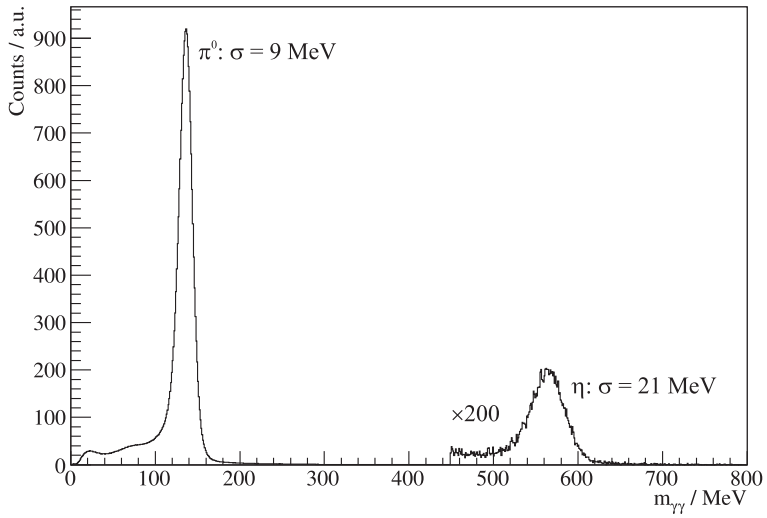

Figure 17: Two photon invariant mass spectrum for the CB/TAPS detector setup. Both η and π^0 mesons can be clearly seen.

The Crystal Ball detector (CB) is a highly segmented 672-element NaI(Tl), self triggering photon spectrometer constructed at SLAC in the 1970's. Each element is a truncated triangular pyramid, 41 cm (15.7 radiation lengths) long. The Crystal Ball has an energy resolution of $\Delta E/E = 0.020 \cdot E[\mathrm{GeV}]^{0.36}$, angular resolutions of $\sigma_\theta = 2 \ldots 3^\circ$ and $\sigma_\phi = \sigma_\theta / \sin\theta$ for electromagnetic showers [24]. The readout electronics for the Crystal Ball were completely renewed in 2003, and it now is fully equipped with SADCs which allow for the full sampling of pulse-shape element by element. In normal operation, the onboard summing capacity of these ADCs is used to enable dynamic pedestal subtraction and the provision of pedestal, signal and tail values for each element event-by-event. Each CB element is also newly equipped with multi-hit CATCH TDCs. The readout of the CB is effected in such a way as to allow for flexible triggering algorithms. There is an analogue sum of all ADCs, allowing for a total energy trigger, and also an OR of groups of sixteen crystals to allow for a hit-multiplicity second-level trigger - ideal for use when searching for high multiplicity final states.

In order to distinguish between neutral and charged particles species detected by the Crystal Ball, the system is equipped with PID, a barrel detector of twenty-four 50 mm long, 4 mm thick scintillators, arranged so that each PID scintillator subtends an angle of 15° in ϕ. By matching a hit in the PID with a corresponding hit in the CB, it is possible to use the locus of the $\Delta E, E$ combination to identify the particle species (Fig. 18). This is primarily used for the separation of charged pions, electrons and protons. The PID covers from 15° to 159° in θ.

The excellent CB position resolution for photons stems from the fact that a given photon triggers several crystals and the energy-weighted mean of their positions locates the photon position to better than the crystal pitch. For charged particles which deposit their energy over only one or two crystals, this is not so precise. Here the tracks of charged particles emitted within the angular and momentum acceptance of the CB detector will be reconstructed from the coordinates of point of intersections of the tracks with two coaxial cylindrical multiwire proportional chambers (MWPCs) with cathode strip readout. These MWPCs are similar to those installed inside the CB during the first round of MAMI-B

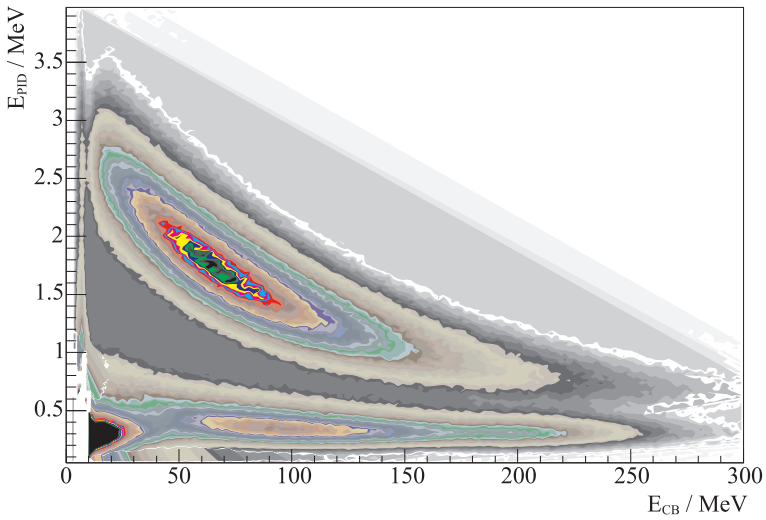

Figure 18: A typical $\Delta E/E$ plot from the Crystal Ball and the PID detector. The upper curved region is the proton locus, the lower region contains the pions and the peak towards the origin contains mostly electrons.

runs [25]. The most significant difference is that all detector signals are taken at the upstream end of the MWPCs, minimising the material required and facilitating particle detection in the forward polar region.

A mixture of argon (79.5%), ethane (30%) and freon-CF_4 (0.5%) is used as the filling gas. This mixture is a compromise between charge multiplication and localization requirements imposed by the ionizing particle tracks.

Within each chamber both the azimuthal and the longitudinal coordinates of the avalanche will be evaluated from the centroid of the charge distribution induced on the cathode strips. The location of the hit wires(s) will be used to resolve ambiguities which arise from the fact that each pair of inner and outer strip cross each other twice. The expected angular resolution (rms) will be $\sim 2^\circ$ in the polar emission angle θ and $\sim 3^\circ$ in the azimuthal emission angle ϕ.

A.5 TAPS Forward Wall

The TAPS forward wall is composed of 384 BaF_2 elements, each 25 cm in length (12 radiation lengths) and hexagonal in cross section, with a diameter of 59 mm. The front of every TAPS element is covered by a 5 mm thick plastic veto scintillator. The single counter time resolution is $\sigma_t = 0.2$ ns, the energy resolution can be described by $\Delta E/E = 0.018 + 0.008/E[\mathrm{GeV}]^{0.5}$ [24]. The angular resolution in the polar angle is better than 1°, and in the azimuthal angle it improves with increasing θ, being always better than $1/R$ radians, where R is the distance in centimeters from the central point of the TAPS wall surface to the point on the surface where the particle trajectory meets the detector. The TAPS readout was custom built for the beginning of the CB@MAMI program and is effected in such a way as to allow particle identification by Pulse Shape Analysis (PSA), Time Of Flight (TOF) and $\Delta E/E$ methods (using the energy deposit in the plastic scintillator to give ΔE). TAPS can also contribute to the CB multiplicity trigger and is currently divided into upto six sectors for this purpose. The 2 inner rings of 18 BaF_2

elements have been replaced recently by 72 $PbWO_4$ crystals each 20 cm in length (22 radiation lengths). The higher granularity improves the rate capability as well as the angular resolution. The crystals are operated at room temperature. The energy resolution for photons is similar to BaF_2 under these conditions [26].

References

[1] M. Tanabashiet *et al.* (Particle Data Group): *Review of Particle Physics*, Phys. Rev. **D 98** (2018 and 2019 update) 030001

[2] V. Sokhoyan *et al.*: *Determination of the scalar polarizabilities of the proton using beam asymmetry Σ_3 in Compton scattering*, Eur. Phys. J. **A 53** (2017) 14

[3] P.P. Martel *et al.*: *Measurements of Double-Polarized Compton Scattering Asymmetries and Extraction of the Proton Spin Polarizabilities*, Phys. Rev. Lett. **114** (2015) 112501

[4] D. Paudyal *et al.*: *Spin polarizabilities of the proton by measurement of Compton double-polarization observables* arXiv:1909.02032 (2019)

[5] J. Schmiedmayer, P. Riehs, J.A. Harvey, and N.W. Hill: *Measurement of the electric polarizability of the neutron*, Phys. Rev. Lett. **66** (1991) 1015

[6] L. Koester, W. Waschkowski, L.V. Mitsyna, G.S. Samosvat, P. Prokofjevs, and J. Tambergs: *Neutron-electron scattering length and electric polarizability of the neutron derived from cross sections of bismuth and of lead and its isotopes*, Phys. Rev. **C 51** (1995) 3363

[7] T.L. Enik, R.V. Kharjuzov, L.V. Mitsyna, and G.S. Samosvat: *The UGRA spectrometer for the measurement of the electric polarizability of the neutron*, Nucl. Inst. Meth. Phys. Res. **A 440** 2000 777

[8] M. Schumacher: *Polarizability of the nucleon and Compton scattering*, Prog. Part. Nucl. Phys. **55** (2005) 567

[9] M.I. Levchuk and A.I. L'vov: *Deuteron Compton scattering below pion photoproduction threshold*, Nucl. Phys. **A 674** (2000) 449

[10] L.S. Myers *et al.*: *Measurement of Compton Scattering from the Deuteron and an Improved Extraction of the Neutron Electromagnetic Polarizabilities*, Phys. Rev. Lett. **113** (2014) 262506

[11] M.A. Lucas: *Ph.D. thesis*, University of Illinois at Urbana-Champaign, 1994

[12] D.L. Hornidge *et al.*: *Elastic Compton Scattering from the Deuteron and Nucleon Polarizabilities*, Phys. Rev. Lett. **84** (2000) 2334

[13] M. Lundin *et al.*: *Compton Scattering from the Deuteron and Extracted Neutron Polarizabilities*, Phys. Rev. Lett. **90** (2003) 192501

[14] D. Wells: *Ph.D. thesis*, University of Illinois at Urbana-Champaign, 1990

[15] K. Fuhrberg *et al.*: *Compton scattering of 87 MeV photons by ^{4}He*, Nucl. Phys. **A 591** (1995) 1

[16] M.H. Sikora *et al.*: *Compton scattering from ^{4}He at 61 MeV*, Phys. Rev. **C 96** (2017) 055209

[17] X. Li *et al.*: *Compton scattering from ^{4}He at HIγS*, arXiv:1912.06915 (2019)

[18] H.W. Grießhammer, J.A. McGovern, D.R. Phillips, G. Feldman: *Using Effective Field Theory to analyse low-energy Compton scattering data from protons and light nuclei*, Prog. Part. Nucl. Phys. **67** (2012) 841

[19] A. Margaryan, B. Strandberg, H.W. Grießhammer, J.A. McGovern, D.R. Phillips, D. Shukla: *Elastic Compton scattering from ^{3}He and the role of the Delta*, Eur. Phys. J. **A 54** (2018) 125

[20] D. Shukla, A. Nogga and D.R. Phillips: *Analyzing the effects of neutron polarizabilities in elastic Compton scattering off ^{3}He*, Nucl. Phys. **A 819** (2009) 98

[21] N.M. Jermann: *M.S. thesis*, University of Basel, Basel Switzerland, 2019

[22] J.C. McGeorge *et al.*: *Upgrade of the Glasgow photon tagging spectrometer for Mainz MAMI-C*, Eur. Phys. J. **A 37** (2008) 129

[23] A. Thomas *et al.*: *The GDH Experiment at MAMI*, Nucl. Phys. **B 79** (1999) 591

[24] S. Prakhov *et al.*: *Measurement of the Slope Parameter α for the $\eta \to 3\pi^0$ decay with the Crystal Ball detector at the Mainz Microtron (MAMI-C)*, Phys. Rev. **C 79** (2009) 035204

[25] G. Audit *et al.*: *DAPHNE: a large-acceptance tracking detector for the study of photoreactions at intermediate energies*, Nucl. Instr. Meth. **A 301** (1991) 473

[26] R. Novotny *et al.*: *Scintillators for photon detection at medium energies: A comparative study of BaF-2, CeF-3 and PbWO-4*, Nucl. Instrum. Meth. A **486** (2002) 131